01

Investigations of Microscopic X-ray tomography

© K.P. Gaikovich, I.V. Malyshev, D.G. Reunov, N.I. Chkhalo

Institute of Physics of Microstructures, Russian Academy of Sciences,
603950 Nizhny Novgorod, Russia
e-mail: gaikovich@mail.ru

Received April 9, 2024
Revised April 9, 2024
Accepted April 9, 2024

As a result of the development of the theory of the geometric-optical approach in X-ray tomography, numerical modeling and optimization based on the results of experimental data, an X-ray tomography algorithm was developed that implements a resolution of $0.14\,\mu$m, exceeding the resolution achievable in optical systems. The method was applied in the tomographic analysis of lily of the valley cells, where numerous small ($0.001-0.003\,\mu\text{m}^{-1}$) absorption inhomogeneities in the form of rings 1–2 pixels thick ($0.14-0.28\,\mu$m) were found, presumably cross sections of the shells of spheroidal bodies. The discovered oblate of the rings in the vertical section allowed us to conclude about the shape of these bodies. In order to distinguish the smallest details in the reconstruction of a plant cell from artifacts, numerical modeling was performed using test objects comparable in absorption and size, which were embedded in the previously obtained cell reconstruction. The results confirmed the above-mentioned resolution with high sensitivity to changes in the absorption coefficient.

Keywords: X-ray microscopy, absorption coefficient, inverse problem, numerical modeling, tomography of plant cells.

DOI: 10.61011/TP.2024.07.58793.114-24

Introduction

A microscopic X-ray tomography method using an X-ray microscope was proposed in [1], where a method was specifically developed and successfully used to solve the inverse problem of tomography. This method solved the problem by means of a 3D integral convolution-type equation that used the calculated sounding field distribution as the kernel. The geometric-optical approach was used in [2] to solve this problem, and an integral equation of the tomography inverse problem was derived explicitly from the Radon transform formalism. Findings of the numerical simulation of solution algorithm for this equation are shown in [2]. The study continues the theoretical investigation of this approach and applications for more detailed plant cell analysis that is necessary in biology and medicine [3].

Optical visible light microscopy does not allow direct examination of the nanostructure of living cells with details less than diffraction blurring [4]. Various methods of increasing the resolution of optical microscopy, for example, fluorescence STED microscopy (Stimulated Emission Depletion Microscopy) [5], are used to significantly exceed the diffraction limit and achieve a resolution of tens of nanometers. However, as in the case of classical fluorescence microscopy, the method can distinguish only tinted organelles isolated from the environment, which makes it difficult to understand the processes taking place in cells. Electron microscopy has a high spatial resolution up to nanometers [6]. However, the studied samples have to be frozen and cut into 100–500 nm films to conduct such studies, i.e. this method is destructive and cannot be used to study whole cells [7]. Atomic force and scanning tunneling microscopy can examine only the surface of the samples.

The approach proposed herein uses the 13.84 nm X-ray microscope developed by the Institute of Physics of Microstructures, Russian Academy of Sciences [1]. Soft X-ray microscopy (SX microscopy) has been developing for more than thirty years in the spectral range of the „water transparency window“, 2.3–4.4 nm wavelengths [8–12], as well as in the extreme ultraviolet (EUV) range at 13.4–13.8 nm [13–20]. The key advantages of the X-ray „water-window“ microscopic testing are as follows:

- short wavelength in the diffraction limit provides nanometer spatial resolution;
- natural absorption contrast between carbon-containing structures and water, which is higher by an order of magnitude or more, allowing samples to be examined without using contrasting and/or fluorescent substances;
- relatively high transmission and almost no scattering of radiation make it possible to study cells and tissue sections up to $10-15\,\mu$m in thickness in their natural, potentially living state;
- sample preparation process is significantly simplified compared with the methods mentioned above.

1. Theory

The study addresses the tomography problem (determining the 3D absorption coefficient inhomogeneity distribution in the test objects) using the equations derived in [2] to

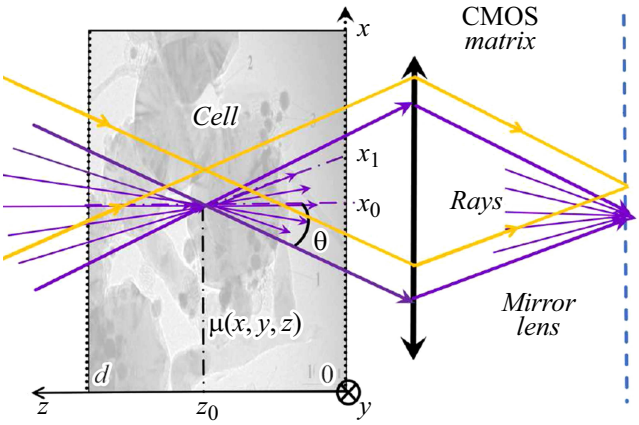

Figure 1. Diagram of the X-ray microscope rays passing through the sample cross section in the focal plane of the lens to the CMOS digital matrix.

the geometrical optics approximation. Figure 1 shows a simplified microscope ray diagram for a model in which a minor beam angle variation within the focus spot in the cell is neglected.

The signal (intensity) at each point of the measuring matrix is formed by all rays in the cone that have passed through the corresponding focus x_0, y_0, z_0 and exit the camera at points $x_1, y_1, z_1 = 0$ in the measuring chamber (Figure 1). At the same time, the mirror lens constructs the image of a sample section caught by the focal plane of the lens. For three-dimensional reconstruction of the sample image, the sample is shifted along the z axis (optical axis of the lens), and a series of $x-y$ images of the sample is recorded by the camera, the so-called z-stack. The scanning grid dimensions in the z plane (pixel size) are determined by the scale of the transverse radiation diffraction spreading in the focus. According to the radiation transfer equation in the absorbing medium, the contribution of each ray to the intensity is defined by the optical absorption thickness — integral of the absorption coefficient along the ray path

$$\tau = \int_L \mu(x, y, z)dl$$

on the straight line passing through points x_0, y_0, z_0 and $x_1, y_1, z_1 = 0$ between the $z = 0$ and $z = d$ planes:

$$J(x_1, y_1, z_1 = 0, x_0, y_0, z_0) = J_0 \exp\left(-\int_L \mu(x, y, z)dl\right). \quad (1)$$

The best known methods of medical tomography — CT (computed tomography) and MRI (magnetic resonance imaging) also give the same equation. These methods are based on the Radon transform theory proposed by Radon in [21] and later developed by A.N. Tikhonov and his colleguas for computed X-ray tomography applications based on the theory of incorrect inverse problems [22–25]. Unlike CT and MRI, this problem provides no imaging capability for the explored object on all sides, and the corresponding Radon transform equations for the addressed microscopic tomography method were obtained in [2]. Summary of the developed theory is provided below.

Using the parametric representation of the optical thickness [2]:

$$\tau(x_1, y_1, z_1, x_0, y_0, z_0) = \\ = \sqrt{(x_0 - x_1)^2 + (y_0 - y_1)^2 + (z_0 - z_1)^2} \\ \times \int_{\lambda_1}^{\lambda_2} \mu\left[x_1 + (x_0 - x_1)\lambda, y_1 + (y_0 - y_1)\lambda, z_1 + (z_0 - z_1)\lambda\right] d\lambda, \quad (2)$$

by replacing $z_0\lambda \to z$, equation (1) may be written in the Cartesian coordinates:

$$J(x_1, y_1, z_1, x_0, y_0, z_0) = J_0 \\ \times \exp\left(-\sqrt{(x_0 - x_1)^2 + (y_0 - y_1)^2 + z_0^2}/z_0 \int_0^d \mu[x_1 \right. \\ \left. + (x_0 - x_1)z/z_0, y_1 + (y_0 - y_1)z/z_0, z]dz\right). \quad (3)$$

Then, by means of integration for all rays in the cone that exit through the plane $z = 0$ and assuming for rays in the focusing area $J_0 = \text{const}$, we get the direct problem solution (Radon transform in the measurement geometry of interest) — relative intensity $I(x_0, y_0, z_0)/I_0[\mu = 0]$ in the matrix point corresponding to the focus position in (x_0, y_0, z_0) point [2]:

$$\frac{I(x_0, y_0, z_0)}{I_0[\mu = 0]} = \int_{x_0 - z_0 \operatorname{tg}\theta}^{x_0 + z_0 \operatorname{tg}\theta} dx_1 \int_{-\sqrt{(z_0 \operatorname{tg}\theta)^2 - (x_0 - x_1)^2}}^{\sqrt{(z_0 \operatorname{tg}\theta)^2 - (x_0 - x_1)^2}} dy_1 \\ \times \exp\left(\frac{\sqrt{(x_0 - x_1)^2 + (y_0 - y_1)^2 + z_0^2}}{z_0} \int_0^d \mu\left[x_1 \right.\right. \\ \left.\left. + \frac{(x_0 - x_1)z}{z_0}, y_1 + \frac{(y_0 - y_1)z}{z_0}, z\right]dz\right) \Bigg/ \int_{x_0 - z_0 \operatorname{tg}\theta}^{x_0 + z_0 \operatorname{tg}\theta} dx_1 \\ \times 2\sqrt{(z_0 \operatorname{tg}\theta)^2 - (x_0 - x_1)^2}. \quad (4)$$

Taking into account an additional condition of smallness of the optical absorption thickness $\tau \ll 1$ used in the solution algorithm [2], we get an expression for the relative decrease

in intensity:

$$\delta I(x_0, y_0, z_0) = [I_0 - I]/I_0$$
$$= \int_{x_0 - z_0 \operatorname{tg}\theta}^{x_0 + z_0 \operatorname{tg}\theta} dx_1 \int_{-\sqrt{(z_0 \operatorname{tg}\theta)^2 - (z_0 - x_1)^2}}^{\sqrt{(z_0 \operatorname{tg}\theta)^2 - (x_0 - x_1)^2}} dy_1$$
$$\times \sqrt{(x_0 - x_1)^2 + (y_0 - y_1)^2 + z_0^2}/z_0 \int_0^d \mu\left[x_1 + (x_0 - x_1)/z_0 \right.$$
$$\left. + y_1 + (y_0 - y_1)z/z_0, z\right] dz \Big/ \int_{x_0 - z_0 \operatorname{tg}\theta}^{x_0 + z_0 \operatorname{tg}\theta} dx_1$$
$$\times 2\sqrt{(z_0 \operatorname{tg}\theta)^2 - (x_0 - x_1)^2}, \quad (5)$$

where the subintegral function μ in the integral for z may be written as the double integral for x and y:

$$\delta I(x_0, y_0, z_0) = \iint dx_1 dy_1 \int_0^d \iint dx dy \, \mu(x, y, z)$$
$$\times K(x_0 - x_1, y_0 - y_1, z_0) \delta\left[x - x_1, (x_0 - x_1)z/z_0\right]$$
$$\times \delta\left[y - y_1, (y_0 - y_1)z/z_0\right] dz, \quad (6)$$

and the function K describing all the points inside the light cone in Figure 1 is introduced into (6) instead of the integration limits and multipliers. The integration order may be further changed and variables $\tilde{x}_1 = x_1(z_0 - z)/z_0$, $\tilde{y}_1 = (z_0 - z)/z_0$ may be replaced in (6), and then by means of integration with the δ function for $\tilde{x}, \tilde{y}$, we derive the sought-for integral 3D convolution tomography equation with kernel K set in the explicit form:

$$\delta I(x_0, y_0, z_0) = [I_0 - I]/I_0 = \int_0^d \iint \mu(x, y, z)$$
$$\times K(x_0 - x, y_0 - y, z_0 - z) dx dy dz, \quad (7)$$

$$K(x_0 - x, y_0 - y, z_0 - z) =$$
$$\left\{ \begin{array}{l} = \dfrac{1}{\pi(\operatorname{tg}\theta)^2 (z_0 - z)^2} \sqrt{\left(\dfrac{x_0 - x}{z_0 - z}\right)^2 + \left(\dfrac{y_0 - y}{z_0 - z}\right)^2 + 1} \\ \text{for } \left|\dfrac{x_0 - x}{z_0 - z}\right| < \operatorname{tg}\theta, \left|\dfrac{y_0 - y}{z_0 - z}\right| < \sqrt{(\operatorname{tg}\theta)^2 - \left(\dfrac{x_0 - x}{z_0 - z}\right)^2} \\ = 0 \text{ for } \left|\dfrac{x_0 - x}{z_0 - z}\right| > \operatorname{tg}\theta, \left|\dfrac{y_0 - y}{z_0 - z}\right| > \sqrt{(\operatorname{tg}\theta)^2 - \left(\dfrac{x_0 - x}{z_0 - z}\right)^2} \end{array} \right\}, \quad (8)$$

where the equation kernel K also includes the radiation finding conditions in the cone. 3D Fourier transform (7) results in a simple equation for spectra in the k-space

$$\delta I(k_x, k_y, k_z) = 8\pi^3 \mu(k_x, k_y, k_z) K(k_x, k_y, k_z), \quad (9)$$

and the equation of the sought-for inverse Radon transform for this tomography method:

$$\mu(x, y, z) = \frac{1}{8\pi^3} \iiint \delta I(k_x, k_y, k_z)/K(k_x, k_y, k_z)$$
$$\times \exp(ik_x x + ik_y y + ik_z) dk_x dk_y dk_z, \quad (10)$$

where for clarity the Fourier transforms use same symbols as in the transformed parameters, so they differ only in their arguments.

The problem of algorithm (7) was the K function singularity in equation (8) in the focus pixel whose size ($0.14\,\mu$m) was chosen in [1] using the calculated scale of the transverse diffraction field spreading in the focus. And the kernel value (8) in this pixel turns to be an uncertain parameter that required additional investigations to make the best choice. In the numerical studies [2], the kernel value in the focus was chosen by averaging its values in the adjacent pixels. Using this value, the algorithm was optimized and the results of the completed numerical simulation are shown in [2]. Since the solution of convolution type inverse problems for input data with error is generally an ill-posed problem (accidental errors may have a wider spatial spectrum than the kernel spectrum resulting in unlimited amplification of small-scale components in the solution), A.N.Tikhonov's method [22] was used for regularization of this problem in the numerical simulation algorithm [2].

2. Experimental and theoretical findings

In 2023 the investigations were continued using both the numerical simulation and the experimental findings obtained on the test sample with the known geometry and large objects with complex internal structure (lily of the valley cells). When using the method for analysis of these complex objects, the algorithm developed in [2] turned to be insufficient for the expected resolution. The problem of algorithm (10) was to choose an uncertain value for K function in its singularity in the focus pixel whose size was defined by the diffraction field spreading scale calculated in [1]. Since this spreading is not described within the geometric-optical approximation used herein, the numerical investigations [2] have chosen the value in the focus by averaging its values in adjacent pixels.

For these investigations, K in the focus was varied and defined by maximizing the observed resolution of fine details in reconstruction of the studied objects and by verification of the achieved resolution in the numerical simulation with control of conformance between the optical thickness of reconstruction and the measured signal attenuation. With such optimization, the kernel peak height (Figure 2, *a*)

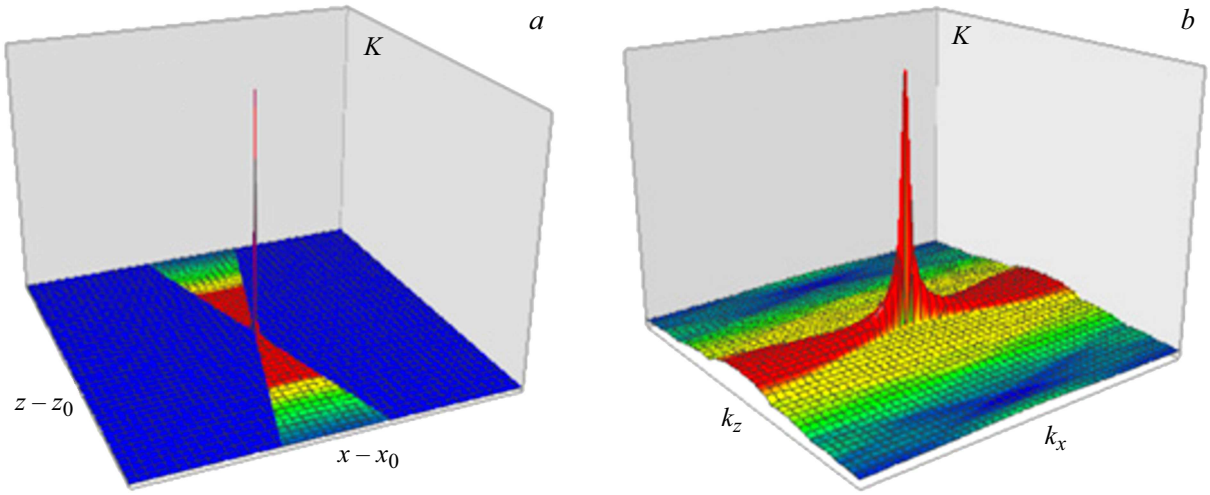

Figure 2. *a* — dimensionless kernel K of equation (6) in section $y = y_0$; *b* — Fourier spectrum modulus of kernel K in equation (8) in the k-space in section $k_y = 0$ at $\theta = 15.65°$.

in the focus turned to grow, algorithm (10) does not require regularization any longer and the tomography results demonstrate much higher resolution.

Figure 2, *b* shows that the kernel peaks form a pedestal in its k spectrum in (10), which ensures the method resolution increase up to the lowest scales corresponding to a single pixel size. This means that the high peak acts as the discrete δ-function that displays the kernel function singularity.

Closed-loop numerical simulation of the modified algorithm was performed for test objects with a given geometric structure (homogeneous objects in terms of the absorption coefficient of parallelepipeds and inhomogeneous objects simulated by the Gaussian distributions:

a) from (7), (8), distribution of the received signal was calculated depending on the focus position in the probing region;

b) „measurement data“ were generated: „measurement error“ with mean zero value and a given level of standard deviation σI was added to the calculated values of the received signal using a random number generator;

c) inverse problem (9), (10) was solved and the calculated value was compared with the given model distribution.

Dependence of the resolution and tomography algorithm accuracy was studied depending on the level of random data errors. Figure 3 shows the reconstruction of a solid test object with sharp boundaries ($20 \times 20 \times 20$ pixel cube) in a dimensionless format with different levels of random error.

Simulation results in Figure 3 show considerable improvement in the reconstruction quality compared with the findings in [2]. Accurate object shape takes place and the algorithm has no error amplification that is typical for ill-posed problems — reconstruction error is proportional to the error level.

When simulating the reconstruction in constant measurement noise level conditions, it was found that the reconstruction error level in vertical sections is a little higher than in vertical sections due to asymmetry of the kernel of equation (7). In the experiments, this effect was enhanced due to the vertical positioning errors. To avoid this factor and decrease the reconstruction error level in further studies, further investigations proposed the method of combining reconstruction data obtained from measurements of an object in two or three perpendicular directions. For the case of reconstruction in three projections, the reconstruction equation is written as:

$$\mu(x, y, z) = \left[\mu_z(x, y, z) + \mu_y(z, x, y) + \mu_x(y, z, x)\right]/3. \tag{11}$$

Figure 4 shows the simulation at a constant measurement noise level of 15% ($\sigma I = 0.15\delta I_{\max}$) in one, two and three projection measurements.

It can be seen in Figure 4 that reconstruction averaging in two projections apparently reduces the error, and averaging in three projections (11) reduces the tomographic testing errors significantly.

The algorithm for solid and distributed absorbing objects with more complex internal structure was investigated. Figure 5 shows the simulation of tomographic reconstruction of a cube $\mu = 1$ with cavity and opening, and of absorption coefficient distribution with cavity based on the difference of two Gaussian functions (horizontal sections through the center of objects in the same coordinates with resolution of 120×128 pixels as in Figure 3).

The figure shows exact reproduction of sharp boundaries of the solid object shapes and of distribution simulated by the Gaussian functions, including the details of 2–4 pixels in size. Proportional dependence of the reconstruction error on the simulated random errors corresponds to the properties of solution of well-posed problems. Note here that solutions of ill-posed inverse problems based on integral equations of the first kind with weak singularities often have correct accurate solution — like, for example, the Abelian transforms used

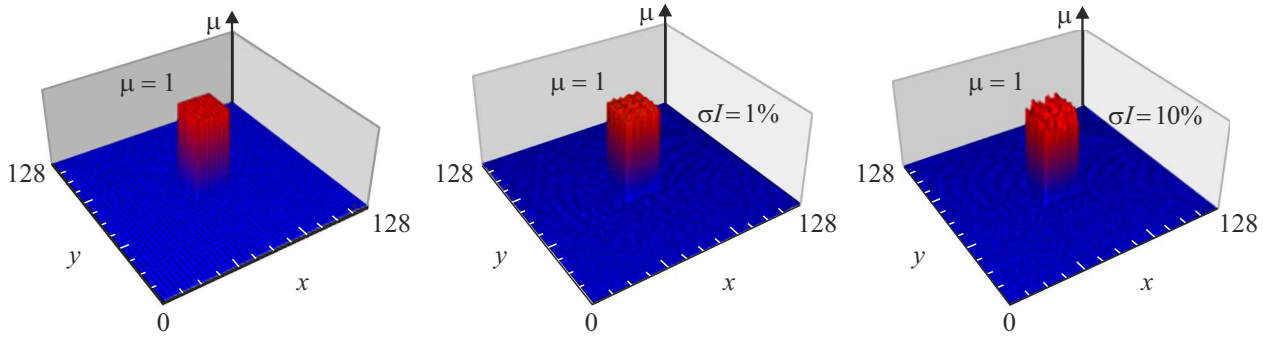

Figure 3. Numerical simulation of tomographic reconstruction. Left — initial distribution in horizontal section $\mu(x, y, z = 64)$; central — reconstruction with random error level $\sigma I = 1\%$; right — at level 10%.

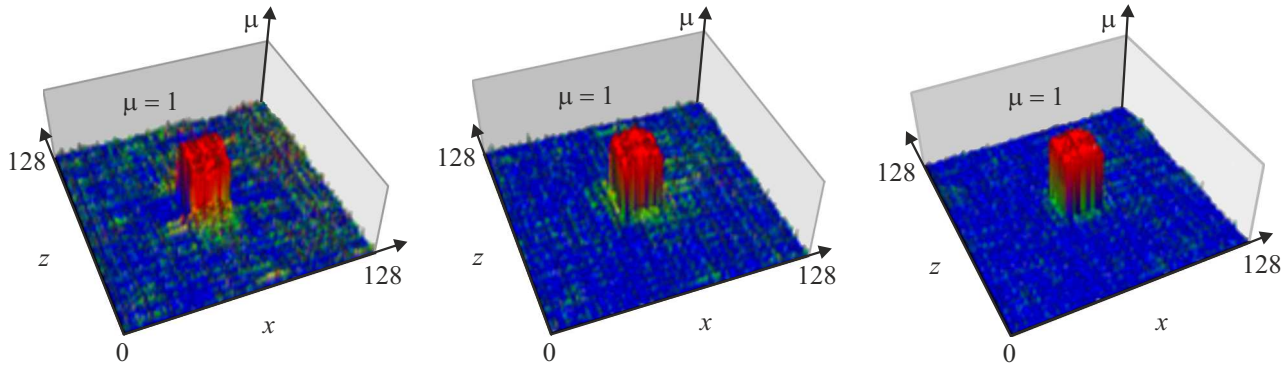

Figure 4. Left — reconstruction by the measurements in one projection in the vertical section $\mu(x, y = 64, z)$; center — in two projections; right — in three projections at level 10%.

in the solution of a set of physical diagnostics problems [26].

However, the problem addressed herein does not deal with accurate solution of the direct problem — it uses geometric-optical minor absorption approximation. Therefore, the correct solution of the problem obtained by numerical simulation using the closed loop as described above does not allow for conclusion that it is efficient for real diagnostics. Such investigations herein were carried out on real objects with quite complex multiscale internal structure — dried plant cells of a lily of the valley stem.

The plant cells were examined with discretization of $256 \times 256 \times 256$ pixels. Figure 6 shows distributions of the measured signal in the horizontal plane through the vertical center of the object at the vertical focus level. Pseudo-three-dimensional grayscale representation was used (the representation of findings hereinafter is chosen on the basis of the most accurate reproduction of image details).

Figure 7, 8 shows the results of tomographic reconstruction of the absorption coefficient distribution of cells as shown in Figure 6 in horizontal and vertical sections. White level corresponds to $\mu = 0.05\,\mu\text{m}^{-1}$.

Tomograms in Figures 7, 8 demonstrate a complex internal structure of absorption coefficient distribution in the lily of the valley stem cells that contains the information that is beyond the reach of other existing diagnostics methods and certainly is interesting for biologists. Cell structures on the images include localized elements in different scales. circular formations are of special interest — beginning from the smallest to distinctly distinguishable circles — such as those in the center in Figure 7, *b*. These circles are presumably the sections of spheroid bodies in the cell. Due to high resolution of the method, the areas of relative transparency of cells where the finest formations are distinguished most clearly were analyzed in more detail and, moreover, this analysis was used to adjust the reconstruction algorithm (9).

As mentioned above, adjustment of the algorithm based on the numerical simulation does not ensure successful diagnostics of real objects. The numerical analysis calculates the simulated measurement data using the same integral relation that is also used for solution of the inverse problem, therefore selection of kernel (7) in the focus may be optimized in such closed scheme achieving the best compliance of the reconstruction with the given absorption distribution. And it was found that accurate reconstruction is achieved in a wide range of kernel peak values. But when using the algorithm for a real cell tomography problem, it was found that the tomography result depends considerably on the chosen kernel peak value because this choice defines the degree of closeness of the used geometric-optical approximation to the real relationship between the received

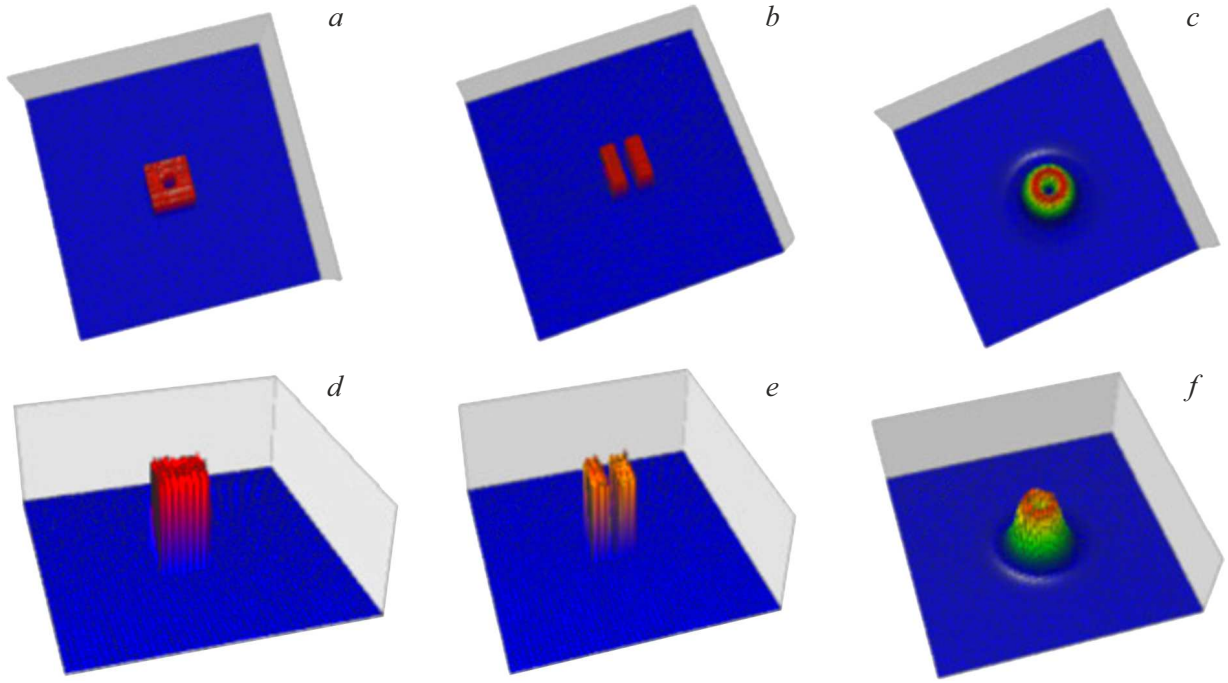

Figure 5. Simulation of reconstruction of various objects (tomographic sections in the horizontal $x-y$ plane through the center of objects with respect to the vertical coordinate z): a, d — $20 \times 20 \times 20$ pixel cube with $4 \times 4 \times 4$ pixel cavity; b, e — $20 \times 20 \times 20$ pixel cube with $4 \times 20 \times 4$ pixel opening through the center of the $x-z$ plane; c, f — absorption coefficient distribution with the internal cavity $\mu(x, y, z) = \exp\left[-\frac{(x-x_c)^2+(y-y_c)^2+(z-z_c)^2}{\sigma_1^2}\right] - \exp\left[-\frac{(x-x_c)^2+(y-y_c)^2+(z-z_c)^2}{\sigma_2^2}\right]$, where the center position $x_c = y_c = z_c = 64$ pixel, and standard deviations $\sigma_1 = 4$ pixels, $\sigma_2 = 2$ pixels. Reconstructions a–c were obtained at the simulated random error level of 1%, and reconstructions d–f were obtained at the error level of 10%.

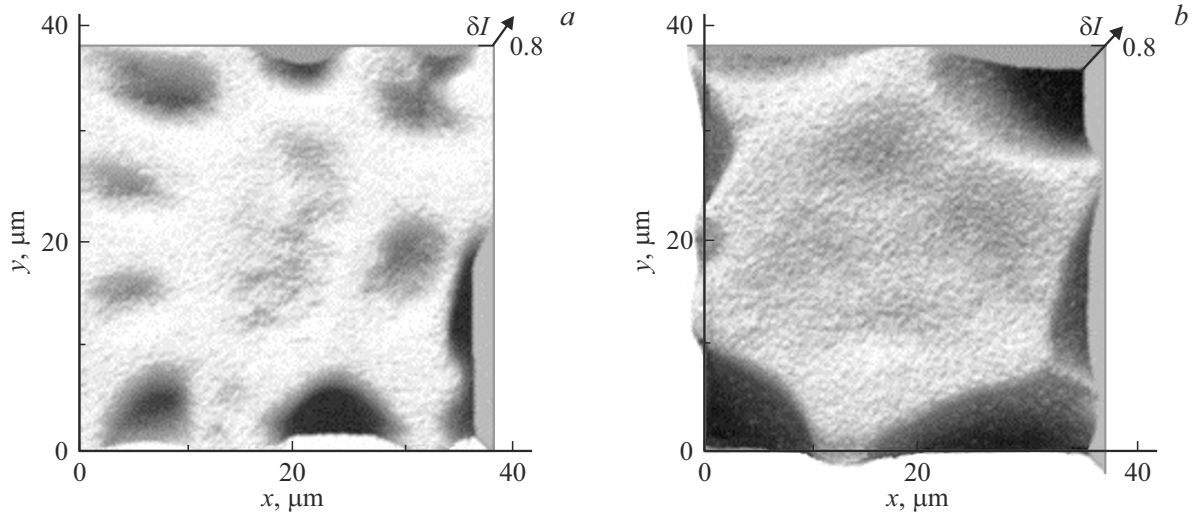

Figure 6. The distribution of the signal from two lily of the valley cells when scanning with a focus in the horizontal plane at the level of the middle of these objects in height.

signal and absorption coefficient distribution. Therefore the peak value was selected herein in such a way as to provide the highest resolution of the finest details in the cell reconstruction structure. At the same time, the correspondence of the largest optical thickness of the cell, estimated by the measured signal, to the optical thickness calculated by the highest absorption coefficient in the reconstruction was checked.

Indirect diagnostics methods based on solution of inverse problems described by integral equations always require that the obtained solution is checked for any artefacts that can simulate the finest details in the reconstruction. Therefore

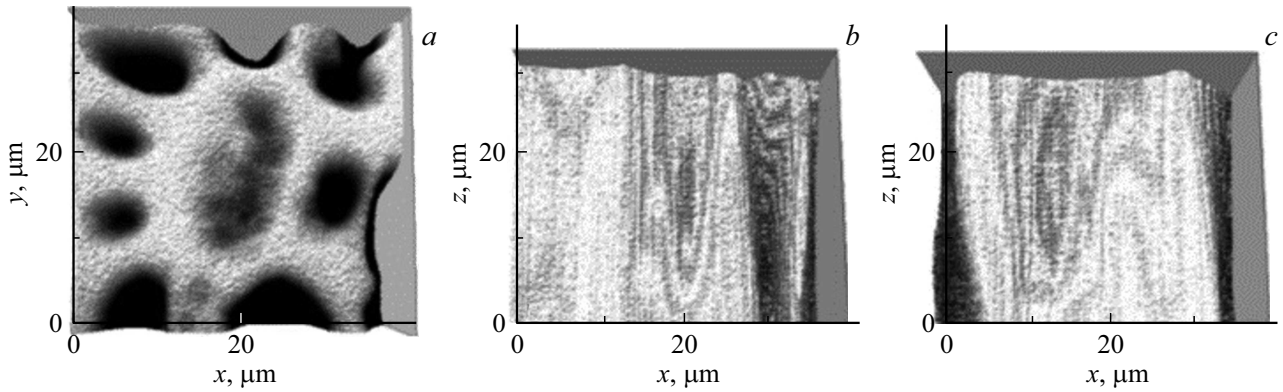

Figure 7. Tomographic analysis of the lily of the valley cell (Figure 6, *a*): *a* — horizontal section in the plane $z = 15\,\mu$m; *b, c* — vertical sections in planes $x = 18\,\mu$m and $y = 18\,\mu$m, respectively.

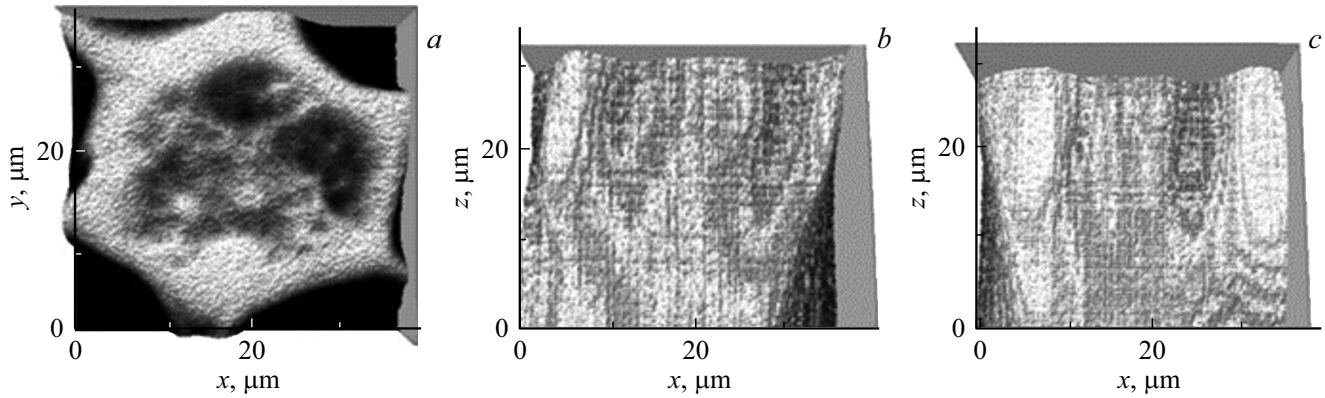

Figure 8. Tomographic analysis of the lily of the valley cell (Figure 6, *b*): *a* — horizontal section in the plane $z = 23\,\mu$m; *b, c* — vertical sections in planes $x = 18\,\mu$m and $y = 18\,\mu$m, respectively.

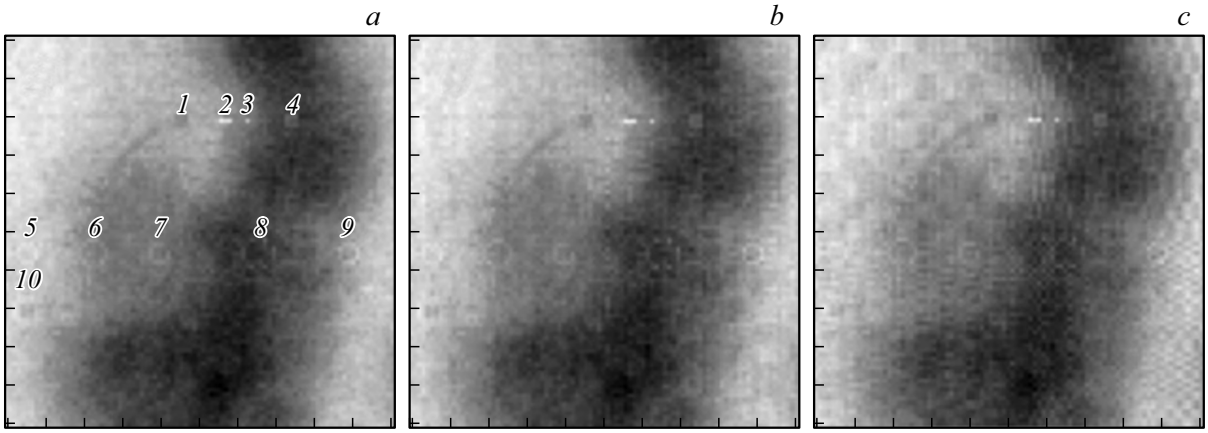

Figure 9. *a* — $12 \times 12\,\mu$m area in the center of cell (Figure 7, *a*) in the horizontal section where sections of the inserted inhomogeneities can be seen: *1, 4* — transparent and absorbing $3 \times 3 \times 3$ pixel cubes; *2* — $3 \times 1 \times 3$ pixel flat object; *3* — single pixel; *5–9* — shells of 3*D* spheroids with radii $R = 2-4$ pixels and thickness $dR = 1$ pixel with absorption $0.001-0.002\,\mu\text{m}^{-1}$; *10* — ball with radius $R = 4$ pixels with transparent cavity and shell with thickness $dR = 2$ pixels; *b* — the same horizontal section of 3*D* distribution reconstruction with inserted inhomogeneities at the error level of 1%; *c* — reconstruction section with error 2%.

to distinguish the finest details in the cell reconstruction from artefacts, numerical simulation was performed using the test objects that were comparable in absorption and sizes and were inserted in the previous cell reconstruction, and then the numerical simulation scheme described above was used to calculate 3*D* distribution of signal, random error

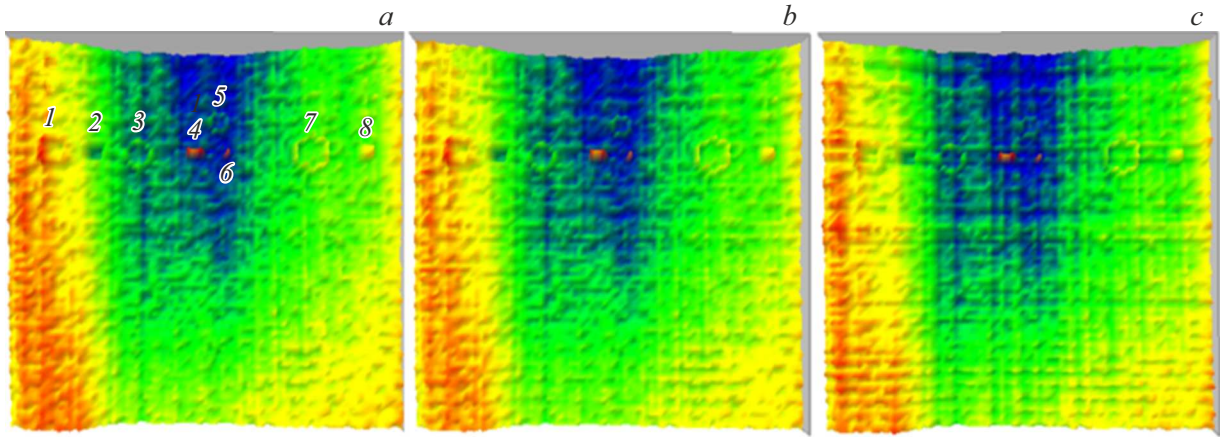

Figure 10. *a* — $12 \times 12\,\mu$m area in the center of cell in Figure 7, *b*) in the vertical section where sections of the inserted inhomogeneities can be seen: *1* — spheroid with radius $R = 4$ pixels and thickness $dR = 2$ pixels; *2* — $3 \times 3 \times 3$ pixel transparent cube, *3* — spherical shell $R = 3$ pixels, $dR = 1$ pixels, *4* — $3 \times 1 \times 3$ pixel flat object, *5* — spherical shell $R = 2$ pixels, $dR = 1$ pixels; *6* — single pixel;*7* — spheroid shell $R = 4$ pixels, $dR = 1$ pixels, *8* — $3 \times 3 \times 3$ pixel cube. *b* — the same vertical section of 3*D* distribution reconstruction with inserted inhomogeneities at the error level of 1%; *c* — reconstruction section with error 2%.

was added and 3*D* tomogram of distribution with inserted inhomogeneities was reconstructed. Such simulation is already suitable to compare the reconstructed distribution with the initial one and opens the potential of algorithm optimization.

Figures 9, 10 show the results of tomographic reconstructions of the selected area of relative transparency in the cell shown in Figure 7 with inserted 3D, 2D and point test inhomogeneities at different levels of simulated random errors.

In the tomographic section in Figure 9a, numerous small absorption inhomogeneities ($0.001-0.003\,\mu\text{m}^{-1}$) are visible — rings (presumably cross-sections of shells of spheroidal bodies) 1–2 pixels thick, as well as (in the left part) a long curl 1–2 pixels thick. The image also shows the sections of 10 inserted inhomogeneities, including spheroids with absorption $0.001-0.002\,\mu\text{m}^{-1}$ compared with that in natural inhomogeneities of the observed circles. It can be seen that the simulated spheroids are really represented by circles in the section, and some of them successfully simulate nearby natural circular objects.

In the tomographic section of the distribution with inhomogeneities reconstructed with error 1% as shown in Figure 9, *b*, all inserted inhomogeneities can be clearly distinguished, including a flat irregularity of 1 pixel in thickness and a single pixel. The result proves that the observed fine inhomogeneities are real, the circles correspond to the spheroid sections, and the resolution of the set algorithm is 1 pixel ($0.14\,\mu$m). Thus, inhomogeneities exceeding the noise level by $0.001-0.002\,\mu\text{m}^{-1}$ may be distinguished in the relative transparency area, which characterizes the absorption coefficient determination accuracy achieved in this experiment.

In the tomographic section absorption distribution reconstructed with error 2% in Figure 9, *c*, the inserted inhomogeneities are still distinguishable when this reconstruction is compared with the initial one, but the noise effect is already comparable with them in magnitude.

Figure 10 shows the results of the similar study of the relative transparency area of $12 \times 12\,\mu$m in the vertical section in Figure 7, *b*. For the most accurate reconstruction of image details, the pseudo-three-dimensional rainbow representation was used. Red level corresponds to $\mu = 0.05\,\mu\text{m}^{-1}$.

Figure 10, *a* shows numerous circles of 1–2 pixels in thickness with absorption $0.001-0.003\,\mu\text{m}^{-1}$, and sections of the eight inserted 3*D* inhomogeneities. It can be seen that most circles are oblate vertically, which indicates the shape of spheroid bodies as close to the vertically oblate ellipse.

In the section of the distribution with inhomogeneities reconstructed with error 1% as shown in Figure 10, *b*, all inserted inhomogeneities can be clearly distinguished, including a flat irregularity of 1 pixel in thickness and a single pixel. The results obtained support the fact that the observed small circular inhomogeneities are real, as confirmed by the modeling in Figure 9, *b*. They also support the resolution and sensitivity of the reconstruction method stated. The results justify the conclusion about the oblate shape of spheroidal bodies based on the comparison of the ring shapes in Figure 9 with their shapes in Figure 10.

In the tomographic section of the absorption distribution reconstructed with error 2% in Figure 10, *c*, the reconstructed inhomogeneities are still distinguishable when this they are compared with the preset ones in Figure 10, a, but some of them almost blend into the background.

Conclusion

The main findings of the study:

1. Development of the theory of geometric-optical approach in the X-ray tomography, numerical simulation and optimization according to the experimental data were used to develop an X-ray tomography algorithm that implements a resolution of $0.14\,\mu$m that exceeds that of the optical methods.

2. This algorithm was used in the tomographic analysis of the lily of the valley cells where numerous fine ($0.001-0.003\,\mu\text{m}^{-1}$) absorption inhomogeneities were found in the form of circles of $1-2$ pixels in thickness ($0.14-0.28\,\mu$m) — presumably spheroid body shell sections. It was also found that these circles are slightly oblate in the vertical tomographic sections suggesting the shape of these spheroid bodies.

3. To distinguish the finest details in the cell reconstruction from artefacts, numerical simulation was performed using the test objects that were comparable in absorption and sizes and were inserted in the previous cell reconstruction, 3*D* distribution of signal of the obtained structure was calculated, random error was added and 3*D* tomogram of distribution with inserted inhomogeneities was reconstructed. Comparison of the reconstructed distribution with the initial one has proved that the resolution of the set algorithm is equal to 1 pixel ($0.14\,\mu$m) with a sensitivity to absorption coefficient variations of $0.001-0.002\,\mu\text{m}^{-1}$.

The findings have demonstrated that the developed X-ray tomography method is suitable for quantitative diagnostics of absorbing cell structures with resolution exceeding the level achievable in the optical systems. But note that the method reconstructions may have errors associated with deviations from the approximation of small absorption, however, these are smooth errors that do not affect the resolution of the most interesting fine details. Future studies are to investigate this aspect in more detail and possibly to find a method of corresponding generalization of the geometric-optical X-ray tomography theory.

Funding

The study was supported by a grant provided by the Russian Science Foundation (Project № 22-62-00068).

Conflict of interest

The authors declare that they have no conflict of interest.

References

[1] I.V. Malyshev, D.G. Reunov, N.I. Chkhalo. Opt. Expr., **30** (26), 47567 (2022). DOI: 10.1364/OE.475032
[2] K.P. Gaikovich, I.V. Malyshev, D.G. Reunov, N.I. Chkhalo. ZhTF, **93** (7), 867 (2023). (in Russian). DOI: 10.21883/JTF.2023.07.55739.106-23
[3] E. Hanssen, C. Knoechel, M. Dearnley, M.W.A. Dixon, M. Le Gros, C. Larabell, L. Tilley. J. Structural Biology, **177** (2), 224 (2012). DOI: 10.1016/j.jsb.2011.09.003
[4] D. Sage, L. Donati, F. Soulez, D.G. Schmit, A. Seitz, R. Guiet, C. Vonesch, M. Unser. Methods, **115**, 28 (2017). DOI: 10.1016/j.ymeth.2016.12.015
[5] G. Vicidomini, P. Bianchini, A. Diaspro. Nat. Methods, **15**, 173 (2018).
[6] V. Lučić, A. Rigort, W. Baumeister. J. Cell Biol., **202** (3), 407 (2013).
[7] K.E. Leigh, P.P. Navarro, S. Scaramuzza, W. Chen, Yi. Zhang, D. Castaño-Díez, M. Kudryashev. Methods Cell Biol., **152**, 217 (2019). DOI: 10.1016/bs.mcb.2019.04.003
[8] P.A.C. Takman, H. Stollberg, G.A. Johansson, A. Holmberg, M. Lindblom, H.M. Hertz. J. Microscopy, **226**, 175 (2007).
[9] C.A. Larabell, M.A. Le Gros. Molecular Biology Cell, **15**, 9572 (2004).
[10] D. Weib, G. Schneider, B. Niemann, P. Guttmann, D. Rudolph, G. Schmah. Ultramicroscopy, **84**, 185 (2000).
[11] M. Bertilson, O. von Hofsten, U. Vogt, A. Holmberg, E. Athanasia, Christakou, H.M. Hertz. Opt. Lett., **36** (14), 2728 (2011).
[12] M. Bertilson, O. von Hofsten, U. Vogt, A. Holmberg, H.M. Hertz. Opt. Expr., **17** (13), 11057 (2009).
[13] M. Toyoda, K. Yamasoe, T. Hatano, M. Yanagihara, A. Tokimasa, T. Harada, T. Watanabe, H. Kinoshita. Appl. Phys. Express, **5** (11), 112501 (2012).
[14] L. Juschkin, R. Freiberger, K. Bergmann. J. Phys.: Conf. Ser., **186**, 012030 (2009).
[15] A. Torrisi, P. Wachulak, Ł. Wegrzyn'ski, T. Fok, A. Bartnik, T. Parkman, Š. Vondrová, J. Tturñová, B.J. Jankiewicz, B. Bartosewicz, H. Fiedorowicz. J. Microscopy, **265** (2), 1 (2016). DOI: 10.1111/jmi.12494
[16] P.W. Wachulak, A. Torrisi, A. Bartnik, Ł. Wegrzyn'ski, T. Fok, H. Fiedorowicz. Appl. Phys. B, **123**, 25 (2017).
[17] T. Ejima, F. Ishida, H. Murata, M. Toyoda, T. Harada, T. Tsuru, T. Hatano, M. Yanagihara, M. Yamamoto, H. Mizutani. Opt. Express, **18** (7), 7203 (2010).
[18] A.V. Vodop'yanov, S.A. Garakhin, I.G. Zabrodin, S.Yu. Zuev, A.Ya. Lopatin, A.N. Nechay, A.E. Pestov, A.A. Perekalov, R.S. Pleshkov, V.N. Polkovnikov. Quantum Electronicsthis, **51** (8), 700 (2021).
[19] I.V. Malyshev, A.E. Pestov, V.N. Polkovnikov, N.N. Salashchenko, M.N. Toropov, N.I. Chkhalo. Poverkhnost. Rentgenovskie, sinkhrotronnye i nejtronnye issledovaniya, **1**, 3 (2019). (in Russian).
[20] N.I. Chkhalo, M.N. Drozdov, E.B. Kluenkov, S.V. Kuzin, A.Ya. Lopatin, V.I. Luchin, N.N. Salashchenko, N.N. Tsybin, S.Yu. Zuev. Appl. Optics, **55** (17), 4683 (2016).
[21] J. Radon. Akad. Wiss., **69**, 262 (1917).
[22] A.N. Tikhonov, V.Ya. Arsenin. *Metody resheniya nekorrektnykh zadach* (Nauka, M., 1986) (in Russian).
[23] A.N. Tikhonov, V.Ya. Arsenin, A.A. Timonov. *Matematicheskie zadachi komp'yuternoj tomografii* (Nauka, M., 1987) (in Russian).
[24] A.N. Tikhonov, A.V. Goncharsky, I.V. Kochikov, E.I. Rau, D.O. Savin, G.V. Spivak, V.V. Stepanov. DAN SSSR, **289** (5), 1104 (1986) (in Russian).
[25] A.N. Tikhonov, P.N. Bochikashvili, A.V. Goncharsky, A.N. Matvienko, E.I. Rau, D.O. Savin, V.V. Stepanov. DAN SSSR, **296** (5), 1095 (1987) (in Russian).
[26] K.P. Gaikovich. *Inverse Problems in Physical Diagnostics* (Nova Science Publishers Inc., NY., 2004)

Translated by E.Ilinskaya